
# Wave ripple development on mixed clay–sand substrates: Effects of clay winnowing and armoring

Wu, Xuxu; Baas, Jaco H.; Parsons, Daniel R.; Eggenhuisen, Joris; Amoudry, Laurent; Cartigny, Matthieu; McLelland, Stuart; Mouazé, Dominique; Ruessink, Gerben

**Journal of Geophysical Research: Earth Surface**

*DOI:*
10.1029/2018JF004681

Published: 01/11/2018

Publisher's PDF, also known as Version of record

Journal of Geophysical Research: Earth Surface

RESEARCH ARTICLE
10.1029/2018JF004681

# Wave Ripple Development on Mixed Clay-Sand Substrates: Effects of Clay Winnowing and Armoring

**Xuxu Wu[1], Jaco H. Baas[2], Daniel R. Parsons[1], Joris Eggenhuisen[3], Laurent Amoudry[4], Matthieu Cartigny[5], Stuart McLelland[1], Dominique Mouazé[6], and Gerben Ruessink[3]**

[1]Department of Geography, University of Hull, Hull, UK, [2]School of Ocean Science, Bangor University, Bangor, UK, [3]Department of Earth Sciences, University of Utrecht, Utrecht, Netherlands, [4]National Oceanography Centre, Liverpool, UK, [5]Department of Geography, Durham University, Durham, UK, [6]Department of Life Sciences and Earth, University of Caen, Caen, France

**Key Points:**
- Relatively small increase of initial bed clay fraction significantly extends time for wave ripples reaching equilibrium
- Clay removal processes facilitate to form sandy equilibrium ripples

**Correspondence to:**
X. Wu,
x.wu@hull.ac.uk

**Citation:**
Wu, X., Baas, J. H., Parsons, D. R., Eggenhuisen, J., Amoudry, L., Cartigny, M., et al. (2018). Wave ripple development on mixed clay-sand substrates: Effects of clay winnowing and armoring. *Journal of Geophysical Research: Earth Surface*, *123*, 2784–2801. https://doi.org/10.1029/2018JF004681

Received 19 MAR 2018
Accepted 4 OCT 2018
Accepted article online 10 OCT 2018
Published online 5 NOV 2018

**Abstract** Based on bed form experiments in a large-scale flume, we demonstrate that the rate of development of wave ripples on a mixed sand-clay bed under regular waves is significantly lower than on a pure-sand bed, even at clay fractions as low as 4.2%, and that this rate of development decreases exponentially from 4.2% to 7.4% clay. These experiments also showed that, despite the slow growth of the bed forms in the mixed sand-clay, the equilibrium length and height of the wave ripples were independent of the initial bed clay fraction. Given that the ripple crests were composed of pure sand at the end of all the experiments that started with well-mixed sand-clay, it is inferred that the clay was removed from the bed during the development of the wave ripples through winnowing into the water column, and possibly also by sieving into the subsurface, where the final clay fractions were found to be higher than the initial clay fractions. These clay removal processes are interpreted to have facilitated the wave ripples to reach equilibrium lengths and heights that are similar to those in pure sand. Clay-carrying pore flow initiated by pressure gradients between the wave ripple troughs and crests might also have contributed to the accumulation of clay in the sediment below the wave ripples. The formation of the clay-enriched "armoring" layer in the substrate is likely to further reduce erosion rates and could influence the dispersion of nutrients and pollutants in coastal seas.

## 1. Introduction

Fluid near the seafloor in coastal and shelf environments experiences wave-induced oscillatory motion if the water depth is sufficiently shallow relative to the length of the waves (Clifton & Dingler, 1984). If the wave-induced bed shear stress exceeds the critical bed shear stress for the initiation of motion of sediment particles, transport of sediment on the seabed takes place. This bed load transport often leads to the generation of wave ripples (Van Rijn, 1993), the size of which is related to the properties of the sediment and the flow, for example, particle size and maximum near-bed orbital velocity (Nelson et al., 2013; Nielsen, 1981; Van Rijn, 1993). Predictive equations allow the dimensions of wave ripples to be determined for known wave parameters (Grant & Madsen, 1982; Grasmeijer & Kleinhans, 2004; Nelson et al., 2013; Pedocchi & Garcia, 2009; Ruessink et al., 2015; Wiberg & Harris, 1994). In geology, the inverse method of predicting wave parameters from known ripple size and sediment size has been used in paleoenvironmental reconstruction (Clifton & Dingler, 1984; Yokokawa, 1995), especially for the approximation of water depth and wave base localization during the time of formation of the wave ripples. Moreover, the time that wave ripples need to adapt to changing wave forcing and thus reach their equilibrium shape and size is essential for determining the roughness of the seabed, which in turn is fundamental to the quantification of dynamic flow-bed feedback processes in local sediment transport models (e.g., Amoudry & Souza, 2011; Bolaños et al., 2012; Li & Amos, 1998; Styles & Glenn, 2002). An improved understanding of these local processes helps to reduce the cumulative errors of sediment transport rate predictions in larger-scale models of, for example, estuarine and shore-face environments. In particular, the height and length of wave ripples are important parameters for the numerical modeling of sediment transport in the marine environment, for example, if the waves resuspend sediment for subsequent transport by currents (Nelson et al., 2013; Perillo et al., 2014; Van Rijn, 2007).

Previous studies have mainly focused on the dynamics of current- and wave-related bed forms on beds composed of pure, well-sorted sand (Baas, 1994, 1999; O'Hara Murray et al., 2011; Schretlen et al., 2009;

Williams et al., 2000, 2004). The size predictors for wave ripples in pure sand have shown that, in general, the height and length of these bed forms increase as the maximum near-bed orbital diameter and the maximum near-bed orbital velocity are increased, and the median particle size on the bed is decreased (e.g., Nielsen, 1981). Considering wave ripples in pure, well-sorted sand only is not a realistic representation of natural sediment in shelf, shore-face, and estuarine environments, where mixed sediments with fine cohesive components are common (Flemming, 2002). Cohesive mixed mud-sand is known to greatly influence bed form characteristics (Baas et al., 2011, 2013) and, in turn, sediment transport rates, because of the formation of flocs and gels of mud that can incorporate sand particles (e.g., Manning et al., 2011; Spearman et al., 2011). Baas et al. (2013) found that small volumes of cohesive clay in sandy substrates significantly slow the rate of current ripple development and that the equilibrium dimensions of these ripples decrease with increasing clay content (Baas et al., 2013). Expanding from the experimental work of Baas et al. (2013), the influence of cohesive clay on the development and stability of ripples formed under regular waves is examined in the present paper. The specific aims were (1) to investigate the relationship between the rate of wave ripple development and the initial bed clay fraction, (2) to determine the equilibrium height and length of these wave ripples as a function of the initial bed clay fraction, and (3) to relate the changing bed composition during bed form development to changes in bed stability, based on the transfer of clay into the water column, that is, clay winnowing, and into the substrate below the bed forms, here referred to as "clay armoring."

## 2. Materials and Methods

### 2.1. Experiment Setup

Five large-scale flume experiments were conducted in the total environment simulator at the University of Hull, United Kingdom. Here a rectangular section of the flume was used (9.8 m long and 1.6 m wide), with a monitoring section at a horizontal distance $x$ = 4.3 m from the wave-generating paddles (Figure 1b) and a perforated board at the end of the flume. The perforated board had a porosity of 15%, and it was mounted at an upstream dipping angle of 6° (Figure 1a) in order to disperse wave energy and thus minimize wave reflections. The sediment bed in the flume was 0.1 m thick at the start of the experiments. All experiments used a mean water depth of 0.6 m, and the salinity of the water was held constant in all runs at ~19 psu, which is typical for estuarine conditions. Experimental run 1 used a bed of well-sorted sand with a median diameter of 496 μm. Wet kaolin clay, which is one of the most common clay types on Earth, was homogenously mixed with the same sand in runs 3 to 6, with the initial clay fraction increasing from 4.2% to 7.4% (Table 1). All the experimental runs were conducted with regular waves with a maximum free-stream orbital velocity, $U_o$, of 0.35 m/s; a wave period, $T$, of 2.48 s; and a wave height, $H$, of 0.2 m, measured using wave gauges (Table 1). Wave orbital velocities were measured with two acoustic doppler velocimeters at 0.03 and 0.41 m above the bed and at a frequency of 25 Hz. Using linear wave theory, these parameters give a wavelength, $L$, of 5.6 m; a maximum near-bed orbital diameter, $A_o$, of 0.14 m; and a mobility number, $\psi$, of 15.8, where

$$\psi = \frac{{U_o}^2}{\left(\frac{\rho_s}{\rho_w} - 1\right) g D_{50}} \tag{1}$$

where $\rho_s$ = 2650 kg/m$^3$ is the sediment density, $\rho_w$ = 1015 kg/m$^3$ is the density of the saline water used in the experiments, $g$ is the constant due to gravity, and $D_{50}$ is the median grain diameter of the sand on the bed. These shallow-water waves had a trochoidal shape.

### 2.2. Procedure

Prior to the start of each run, the bed was wetted, fully homogenized using a handheld concrete mixer, and then flattened using a wooden leveler. Furthermore, syringe-type sediment cores with a diameter of 20 mm and a maximum length of 90 mm were collected at seven equally spaced locations at 3.4 m $< x <$ 9.4 m and at 0.4 m from the right-lateral side of the channel for subsequent grain size analysis using the Malvern Mastersizer 2000 at Bangor University (Figure 1b). Figure 2 shows that none of the initial flat beds had a consistent vertical trend in the sand fraction, suggesting that the clay was well mixed into the sand. After initiating the waves, the development of the bed forms on the initial flat bed was monitored in three dimensions by means of an ultrasonic ranging system (URS). The array contained eight probes, mounted in the center of the monitoring section perpendicular to the wave propagation direction. One probe failed to work in some experiments, so the

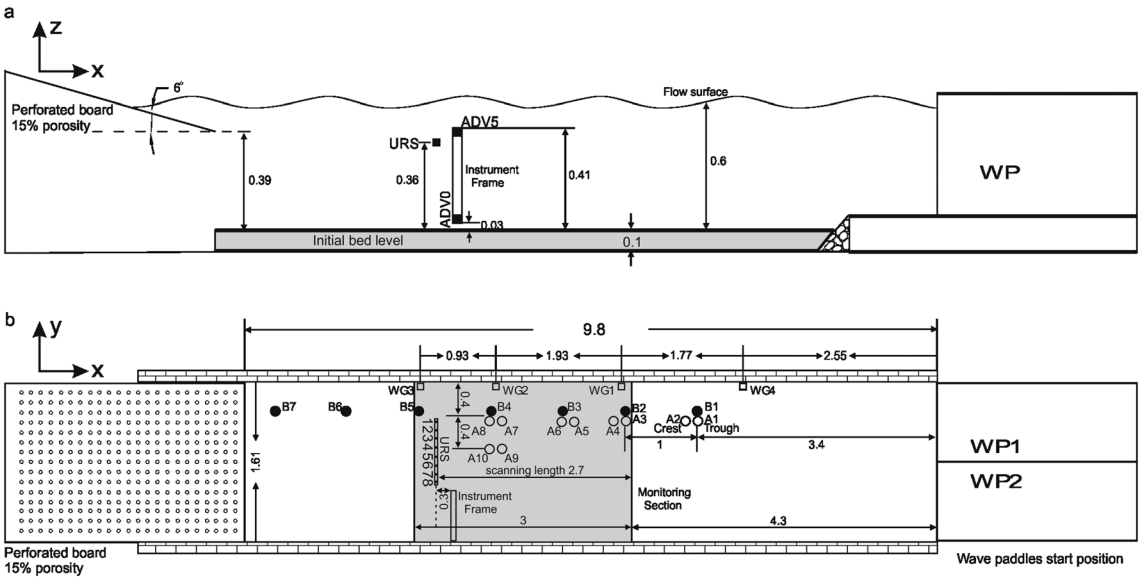


**Figure 1.** (a) Side view and (b) plan view of the experimental setup. The location of the scanning area is shown in gray (with probe numbers), as well as the locations of the sediment cores collected before (black circles) and after (white circles) each run. URS denotes ultrasonic ranging system. WG and WP denote wave gauge and wave paddle, respectively. The shaded area delimits the 3-m long monitoring area. The unit is meter.

3-D scans in these experiments are based on seven sensors. This did not significantly influence the results. The length, width, and speed of data acquisition of the bed scans were 2.7, 0.5, and ~9.3 mm/s, respectively (Figure 1b). The wave generator was stopped every 30 min (except for the first hour of runs 1, 3, and 4, when the wave generator was stopped every 15 min) to allow a bed scan to be completed in standing water. After each run, the water was drained slowly from the tank, and syringe-type sediment cores were taken a second time in order to compare the granulometry of the final bed sediment with that of the initial flat bed at a vertical resolution of 10 mm. These cores were collected from the crest and the trough of the wave ripples at 3.4 m $< x <$ 6.4 m and at 0.4 and 0.8 m from the right-lateral side of the channel (Figure 1b).

### 2.3. Postprocessing of Data

Each acoustic sensor recorded one bed elevation profile (BEP) along the traverse during each scanning period, thus adding up to 7 or 8 BEPs per scan. First, outliers in the BEPs were removed, based on $dz > 5\ dz_m$, where $dz$ is the vertical distance between consecutive data points in the BEP and $dz_m$ is the mean vertical distance in the BEP. Second, any overall linear trend in these BEPs was removed, resulting in a zero mean height

**Table 1**
*Experimental Parameters*

| Run | Duration (min) | Water temperature (°C) | Initial clay fraction[a] (%) | Salinity (‰) | $D_{50}$ (μm) | $H$ start (m) | $H$ End (m) | $U_{won}$[b] start (m/s) | $U_{won}$ end (m/s) | $U_{woff}$ start (m/s) | $U_{woff}$ end (m/s) | $U_{\infty on}$ start (m/s) | $U_{\infty on}$ end (m/s) | $U_{\infty off}$ start (m/s) | $U_{\infty off}$ end (m/s) |
|---|---|---|---|---|---|---|---|---|---|---|---|---|---|---|---|
| 1 | 290 | 16.3 | 0 | 17.8 | 496 | 0.16 | 0.15 | 0.30 | 0.30 | 0.25 | 0.24 | 0.36 | 0.35 | 0.32 | 0.31 |
| 3 | 300 | 15.4 | 4.2 | 19.2 | 457 | 0.22 | 0.19 | 0.31 | 0.31 | 0.26 | 0.26 | 0.36 | 0.36 | 0.31 | 0.30 |
| 4 | 250 | 15.4 | 6.2 | 17.2 | 435 | 0.22 | 0.21 | 0.29 | 0.28 | 0.27 | 0.27 | 0.37 | 0.36 | 0.31 | 0.30 |
| 5 | 510 | 14.6 | 7.2 | 20.4 | 431 | 0.24 | 0.19 | 0.29 | 0.31 | 0.26 | 0.26 | 0.35 | 0.33 | 0.32 | 0.28 |
| 6 | 420 | 15.9 | 7.4 | 19.1 | 421 | 0.21 | 0.21 | 0.29 | 0.29 | 0.25 | 0.23 | 0.35 | 0.33 | 0.31 | 0.30 |

$D_{50}$: median particle size.
$H$: wave height.
$U_{won}$: ADV-derived maximum near-bed onshore orbital velocity.
$U_{woff}$: ADV-derived maximum near-bed offshore orbital velocity.
$U_{\infty on}$: ADV-derived maximum onshore free stream velocity.
$U_{woff}$: ADV-derived maximum offshore free stream velocity.
[a]Dry weight percentage. [b]Onshore flow is defined as toward the perforated plate.

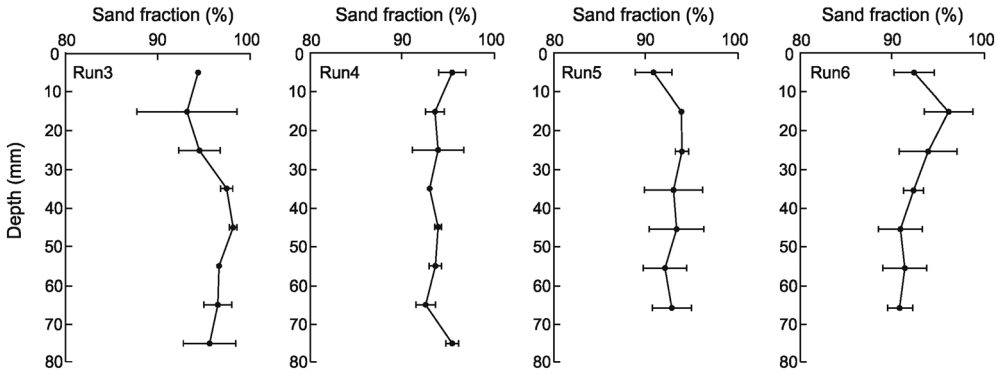


**Figure 2.** Vertical profiles of averaged bed sand fraction in cores collected before each run. The horizontal black lines denote one standard deviation around the mean.

of the bed. Third, each profile was smoothed using a seven-point moving average. Finally, the smoothed BEPs were processed in Matlab using the Van Der Mark bed form tracking tool BTT (Van der Mark et al., 2008). The BTT script determines the locations of wave ripple crests and troughs using the zero-crossing method and then calculates the geometric properties of individual bed forms. The Van der Mark et al. (2008) method locates bed form crests between zero up crossings and zero down crossings. For the present data, however, some crests were not located between two zero crossing points because of long wave length bed level fluctuations. These bed level fluctuations, which resembled nodes and antinodes, probably resulted from minor wave reflections off the perforated plate at the end of the flume and subsequent interference with incident waves (Figure 3). In these cases, the wave ripple lengths and heights were calculated manually. In order to exclude any influence on wave ripple development of turbulent eddies generated around the instrument frame (Figure 1b), average wave ripple lengths and heights were calculated only between 0.7 and 2.7 m in the scanning area (Figure 1b), before being used to construct development curves of wave ripple length and height for each run.

Equilibrium wave ripple heights and lengths were determined using the Baas et al. (2013) method developed for current ripples:

$$\frac{\lambda_t - \lambda_0}{\lambda e - \lambda_0} = 1 - (0.1)^{\frac{t-t_f}{T_\lambda - t_f}} \tag{2}$$

$$\frac{\eta_t}{\eta_e} = 1 - (0.1)^{\frac{t-t_f}{T_\eta - t_f}} \tag{3}$$

where $\lambda_t$ and $\eta_t$ are average wave ripple length and height derived from the BTT at time $t$ after the start of the experiment, $t_f$ is the delay time of wave ripple appearance on the initial flat bed, $\lambda_e$ and $\eta_e$ denote equilibrium wave ripple length and height, $\lambda_0$ is the mean length of the first wave ripples appearing on the flat bed, and $T_\lambda$ and $T_\eta$ are the times needed to reach 90% of the equilibrium bed form length and height. The Curve Fitting Tool in Matlab was used to find the nonlinear best fit solution for equations (2) and (3), thus obtaining $\lambda_e$, $\eta_e$, $\lambda_0$, $T_\lambda$, and $T_\eta$. The delay time, $t_f$, was estimated as the mean of the time of the last flat bed recording—which was $t = 0$ in the runs with a weakly cohesive bed—and the time of the first wave ripple recording on the URS-generated 3-D bed profiles (Table 2). The delay time was zero in noncohesive control run 1. The best fit lines based on equations (2) and (3) describe the experimental data well. The $r^2$ values together with all fitted parameters are shown in Table 2.

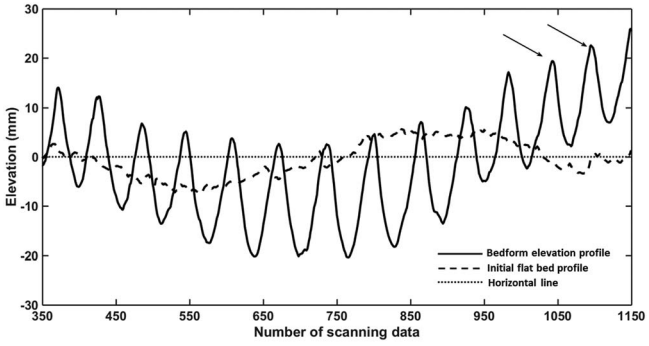


**Figure 3.** Example of a bed form elevation profile (continuous curve) and a corresponding initial bed profile (dashed curve; run 3, $t$ = 240 min), used to identify bed form crests using the zero-crossing method of Van der Mark et al. (2008). The two crests highlighted by the arrows were ignored by the BTT script and were processed manually instead.

## 3. Experimental Results

### 3.1. Wave Ripple Development

In control run 1, conducted with pure sand, wave ripples appeared on the initial flat bed virtually instantaneously, and the entire bed beneath the

**Table 2**
*Fitting Parameters for Wave Ripple Development in Equations (2) and (3)*

| Run | Probe | $T_\lambda$ (min) | $\lambda_e$ (mm) | $\lambda_e$ std (mm) | $\lambda_0$ (mm) | $r^2(\lambda)$ | $T_\eta$ (min) | $\eta_e$ (mm) | $\eta_e$ std (mm) | $r^2(\eta)$ | $t_f$ (min) |
|---|---|---|---|---|---|---|---|---|---|---|---|
| | 1 | 41 | 137.6 | 2.3 | 88.1 | 0.88 | 25 | 20.2 | 0.5 | 0.99 | - |
| | 3 | 38 | 135.5 | 2.4 | 82.3 | 0.86 | 30 | 19.8 | 0.9 | 0.98 | - |
| | 4 | 41 | 135.5 | 2.1 | 80.0 | 0.92 | 26 | 19.4 | 0.5 | 0.99 | - |
| 1 | 5 | 35 | 135.1 | 2.3 | 95.6 | 0.77 | 24 | 20.1 | 0.7 | 0.99 | - |
| | 6 | 34 | 135.6 | 4.5 | 98.0 | 0.60 | 19 | 19.4 | 0.6 | 0.99 | - |
| | 7 | 45 | 135.7 | 4.3 | 75.6 | 0.82 | 33 | 20.1 | 0.7 | 0.99 | - |
| | 8 | 43 | 136.1 | 4.1 | 93.0 | 0.71 | 30 | 19.9 | 0.4 | 0.99 | - |
| | 1 | 58 | 138.1 | 4.6 | 106.5 | 0.77 | 18 | 20.8 | 0.7 | 0.98 | 7 |
| | 3 | 67 | 137.0 | 3.1 | 110.0 | 0.76 | 20 | 19.8 | 0.7 | 0.98 | 7 |
| | 4 | 62 | 138.3 | 3.0 | 108.3 | 0.87 | 15 | 20.1 | 0.4 | 0.99 | 7 |
| 3 | 5 | 60 | 138.5 | 3.2 | 108.7 | 0.88 | 20 | 20.4 | 0.5 | 0.99 | 7 |
| | 6 | 65 | 137.5 | 3.7 | 105.8 | 0.84 | 26 | 19.5 | 0.8 | 0.98 | 7 |
| | 7 | 72 | 138.8 | 4.3 | 92.5 | 0.89 | 39 | 20.9 | 0.8 | 0.98 | 7 |
| | 8 | 77 | 141.2 | 5.1 | 76.5 | 0.93 | 53 | 20.5 | 0.9 | 0.98 | 7 |
| | 1 | 59 | 137.0 | 7.1 | 95.0 | 0.82 | 39 | 20.5 | 1.7 | 0.96 | 15 |
| | 3 | 84 | 135.1 | 3.0 | 81.6 | 0.98 | 76 | 19.6 | 0.8 | 0.99 | 30 |
| | 4 | 140 | 136.7 | 2.9 | 117.8 | 0.96 | 86 | 19.8 | 0.8 | 0.99 | 55 |
| 4 | 5 | 133 | 136.8 | 8.7 | 94.3 | 0.93 | 82 | 19.7 | 0.7 | 0.99 | 55 |
| | 6 | 107 | 133.7 | 6.1 | 95.0 | 0.84 | 91 | 19.1 | 1.1 | 0.99 | 55 |
| | 7 | 134 | 134.1 | 8.5 | 109.0 | 0.68 | 80 | 19.8 | 1.0 | 0.99 | 55 |
| | 8 | 76 | 131.8 | 4.1 | 89.2 | 0.98 | 75 | 19.1 | 1.4 | 0.98 | 30 |
| | 1 | 145 | 136.1 | 3.6 | 106.1 | 0.75 | 54 | 20.1 | 0.5 | 0.97 | 15 |
| | 3 | 120 | 136.1 | 2.3 | 97.9 | 0.88 | 101 | 19.8 | 0.4 | 0.98 | 45 |
| 5 | 4 | 175 | 136.7 | 3.2 | 102.0 | 0.67 | 128 | 19.9 | 0.4 | 0.97 | 75 |
| | 5 | 209 | 139.6 | 3.6 | 122.0 | 0.58 | 104 | 19.9 | 0.7 | 0.98 | 75 |
| | 6 | 187 | 141.2 | 4.0 | 108.5 | 0.76 | 137 | 19.8 | 0.6 | 0.98 | 105 |
| | 7 | 198 | 141.0 | 3.3 | 107.8 | 0.85 | 150 | 21.7 | 0.5 | 0.99 | 105 |
| | 8 | 253 | 143.7 | 4.4 | 119.5 | 0.71 | 169 | 20.7 | 0.3 | 0.98 | 105 |
| | 1 | 131 | 142.3 | 2.6 | 89.4 | 0.97 | 63 | 20.9 | 0.6 | 0.99 | 15 |
| | 3 | 132 | 141.3 | 3.3 | 109.6 | 0.85 | 65 | 20.1 | 0.6 | 0.99 | 45 |
| | 4 | 178 | 144.2 | 5.0 | 98.7 | 0.92 | 69 | 19.7 | 0.8 | 0.97 | 45 |
| 6 | 5 | 146 | 141.3 | 2.5 | 112.8 | 0.92 | 134 | 20.0 | 1.2 | 0.97 | 45 |
| | 6 | 265 | 143.2 | 7.2 | 110.5 | 0.89 | 161 | 19.7 | 1.1 | 0.98 | 75 |
| | 7 | 284 | 143.8 | 6.7 | 102.4 | 0.95 | 172 | 20.1 | 1.5 | 0.96 | 105 |
| | 8 | 262 | 140.1 | 7.3 | 98.4 | 0.92 | 189 | 18.6 | 1.9 | 0.95 | 105 |

std: standard deviation.
$r^2$: squared correlation coefficient of the best fit curve.

URS traverse was covered by wave ripples at $t$ = 10 min. The first bed scan, performed at $t$ = 20 min, confirms this visual observation (Figure 4). These wave ripples had symmetrical outlines and straight continuous crest lines, and they persisted until the end of the experiment.

Time series of the development of the mean length and height of the wave ripples in run 1, as well as the standard deviation of the mean for each time instant, are shown in Figure 4. The mean ripple length and height were 125 and 16 mm at $t$ = 20 min. The relatively high standard deviations at this time match the observation that the wave ripples were at different stages of development. The wave ripples grew at a relatively fast rate until $t$ = 50 min; thereafter, the ripple length and height were more stable with generally low standard deviations (Figure 5). Equations (2) and (3) predict equilibrium times for ripple length and height of 40 and 27 min, respectively. The corresponding equilibrium ripple length and height were 136 and 20 mm (Table 2). At the imposed wave conditions and for the 0.496-mm sand, these wave ripples can be classified as orbital ripples (Malarkey & Davies, 2003; Wiberg & Harris, 1994).

Runs 3 to 6 investigated the development of wave ripples on a flat mixed sand-clay bed at progressively higher clay fractions (Table 1). Representative examples of the development of the wave ripples for run 3 (lowest clay fraction: 4.2%) and run 6 (highest clay fraction: 7.4%) are displayed in Figures 6–9.

Run 3 exhibited a lower wave-ripple growth rate than pure-sand run 1. After 15 min, approximately two thirds of the scanned bed was covered with two-dimensional wave ripples (Figure 6). Thereafter, the waves also

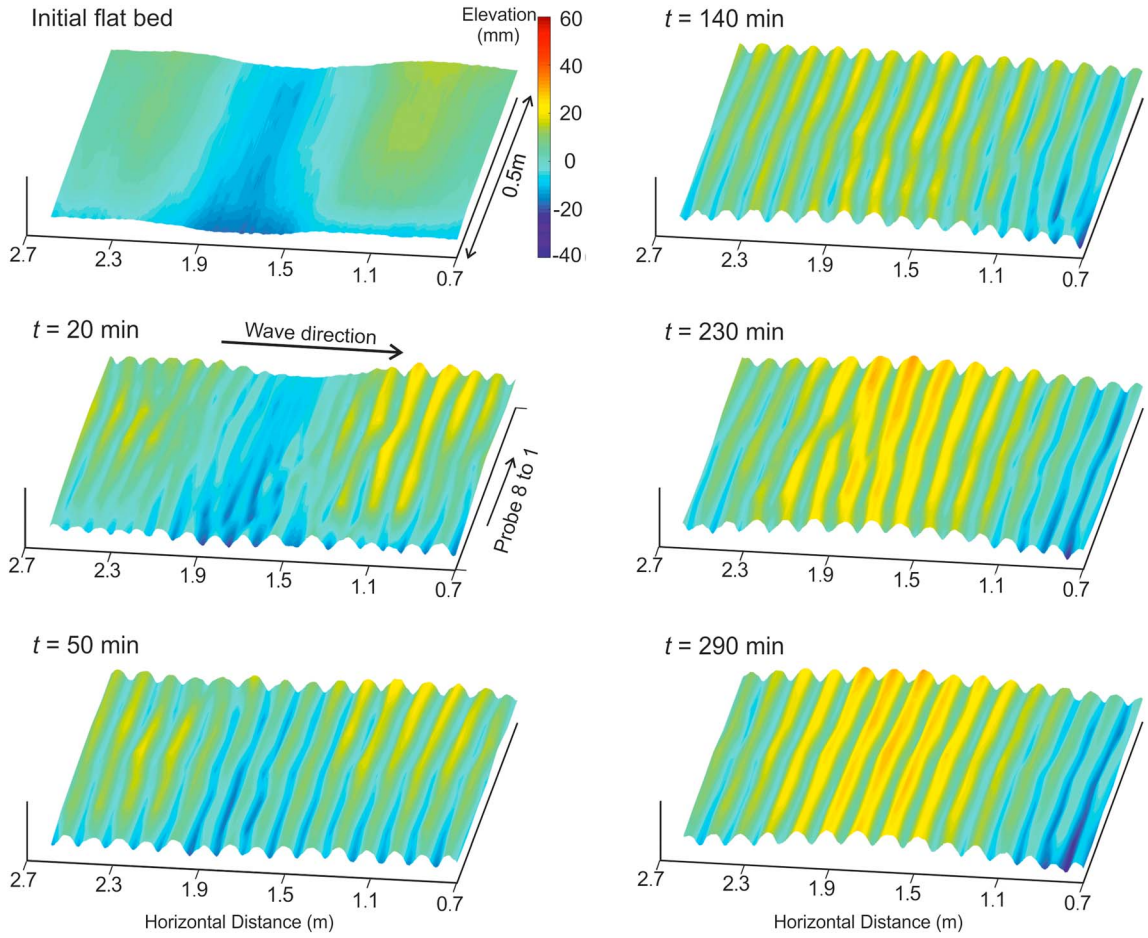


**Figure 4.** Three-dimensional bed scans showing the development of wave ripples in run 1 with pure sand.

reshaped the remainder of the bed into wave ripples until the entire bed was covered by wave ripples at $t$ = 30 min (Figure 6). As in run 1, these wave ripples were straight-crested, and asymmetrical in vertical cross section parallel to the wave propagation direction, and they were present until the end of the run at $t$ = 300 min.

Figure 7 depicts progressive stages of ripple development in run 3. In the first 15 min, wave ripples developed mainly in the middle of the scanned bed, with the URS probes 2 to 6 recording a mean ripple length of ~120 mm, and probes 1, 7, and 8 measuring mean ripple lengths less than 110 mm. The estimated delay time for the first wave ripples appearing on the initial flat bed was 7 min (Table 2). The ripples below probes 7 and 8 caught up quickly in the next 45 min, so that after $t$ = 60 min, wave ripple length reached 130–140 mm (Figure 7). Best-fit equation (2) predicts an equilibrium ripple length of 138 mm and an equilibrium time of 66 min (ranging from 58 min below probe 1 to 77 min below probe 8; Table 2). As in run 1, the standard deviation of mean ripple length was larger during bed form development toward equilibrium than during equilibrium conditions.

Wave ripple height in run 3 developed in a similar way as wave ripple length, with the exception that the equilibrium height was reached earlier than the equilibrium length (Figure 7). Despite a large difference in equilibrium time between the URS probes, ranging from 15 min below probe 1 to 53 min below probe 8, the equilibrium height was close to 20 mm below all probes (Table 2).

The wave ripples in run 6 grew in a more irregular way than in runs 1 and 3. The first wave ripples appeared below URS probe 1 at $t$ = 30 min (Figure 8). The wave ripples then expanded onto the adjacent flat bed toward the opposite side of the scanned area while gradually evolving into continuous trains in the next 90 min. Therefore, the delay time for the formation of the first wave ripples varied greatly,

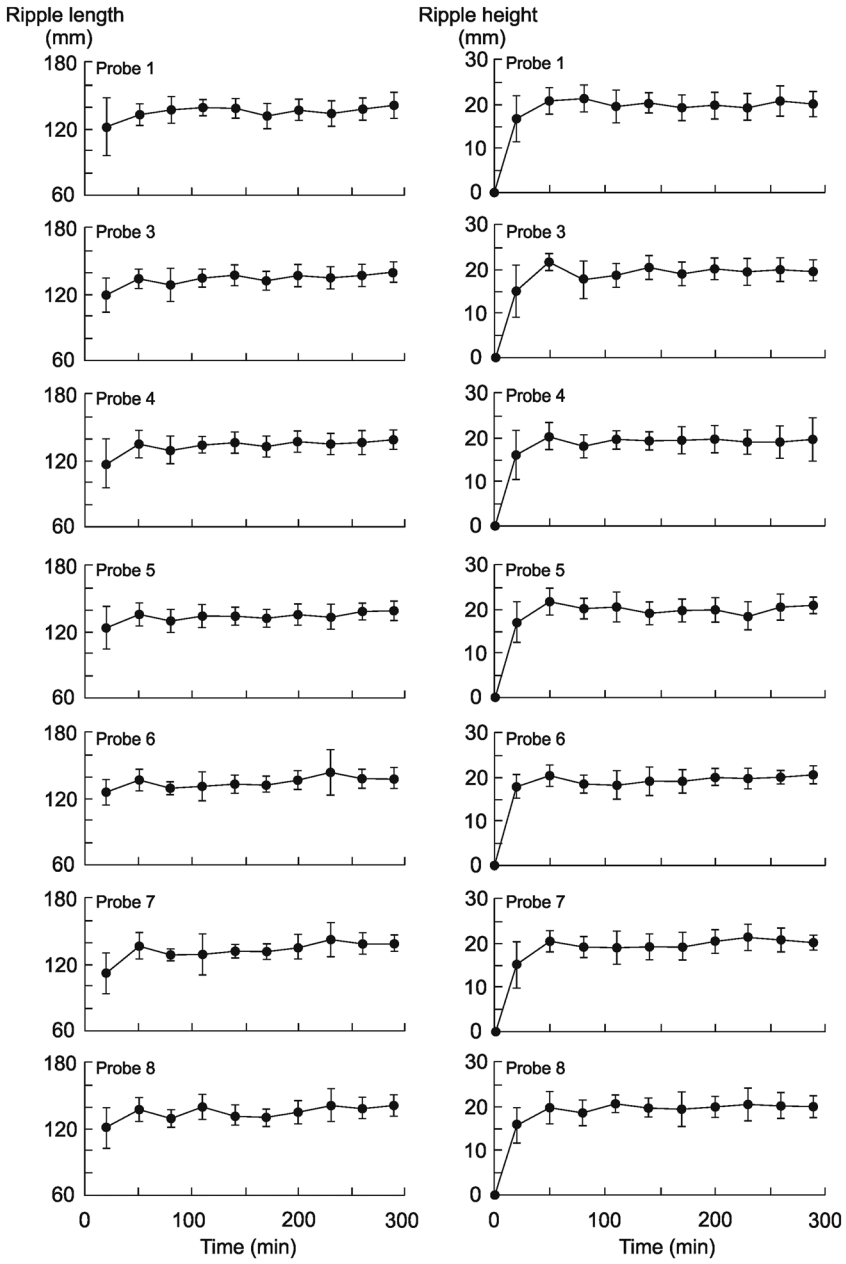


**Figure 5.** Development curves of wave ripple length and height in pure-sand run 1. The vertical black lines denote one standard deviation of the mean.

from $t$ = 15 min below probe 1 to $t$ = 105 min below probe 8 (Table 2). At $t$ = 180 min, most of the bed was occupied by straight-crested 2-D wave ripples, which then remained until the end of the run at $t$ = 420 min (Figure 8).

The slow expansion of the wave ripples in run 6 is reflected in a large variation in bed form length during development toward equilibrium conditions and higher standard deviations of the mean length than in runs 1 and 3 (Figure 9). The first wave ripples beneath probe 1 at $t$ = 30 min had a mean length of 104 mm. The length of the first wave ripples beneath probe 8 at $t$ = 120 mm was similar at 108 mm, but by this time, the ripples beneath probe 1 had grown to a length of 134 mm. As a consequence, the fitted equilibrium time for ripple length varied greatly among the URS probes, ranging from 131 min for the ripples beneath probe 1 to 284 min for the ripples below probe 7 (Table 2). However, the difference in equilibrium ripple length among the probes was small, ranging from 140 to 144 mm (Table 2).

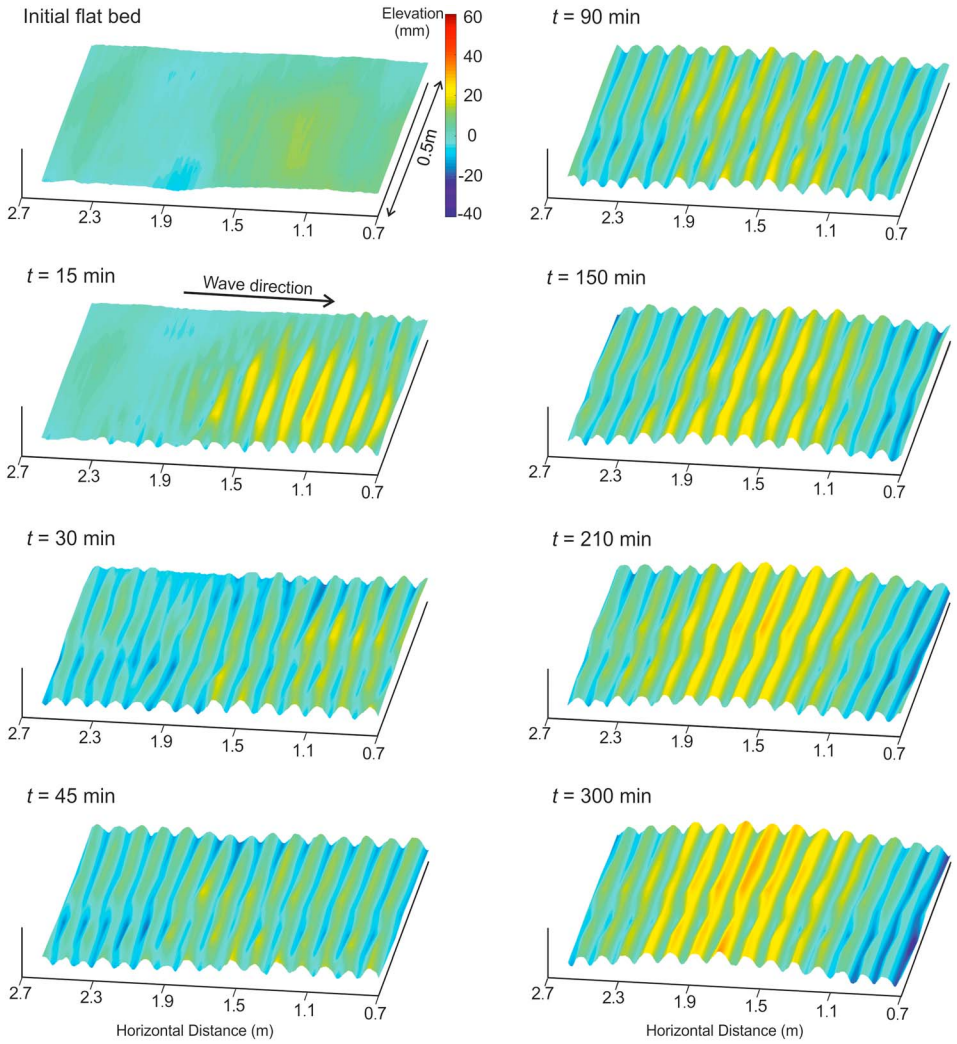


**Figure 6.** Three-dimensional bed scans showing the development of wave ripples in run 3 with 4.2% clay.

The development pattern of wave ripple height mimicked that of wave ripple length, with the early ripples at $t$ = 30 min beneath probe 1 comprising a height of 11 mm, reaching equilibrium height below this probe at $t$ = 63 mm, whereas it took 189 min to reach equilibrium ripple height beneath probe 8 (Table 2 and Figure 9). As for ripple length, the equilibrium ripple height was more consistent than the equilibrium time. The equilibrium ripple height ranged from 19 mm below probe 8 to 21 mm below probe 3 (Figure 9).

### 3.2. Bed Form Equilibrium State Against Initial Clay Fraction

Figure 10 shows the relationship between the initial bed clay fraction and the main properties of the equilibrium wave ripples. The equilibrium length and height of the wave ripples were almost independent of the initial bed clay fraction, ranging from 135.9 to 142.3 mm and from 19.7 to 20.3 mm, respectively (Figures 10a and 10b). The equilibrium wave ripples in the high-clay fraction runs 5 and 6 were marginally longer than at lower bed clay fractions (Figure 10a), but the maximum difference of 6 mm was well within one standard deviation of the length measurements (cf. Figures 7 and 9).

In contrast to equilibrium ripple length and height, the mean equilibrium time of ripple length and height increased exponentially, as the initial bed clay fraction was increased from 0% to 7.4% (Figures 10c and 10d). Reaching equilibrium ripple dimensions on a bed with 7.4% clay required 5 times longer than on a bed without clay. Whereas 40 and 27 min were required to reach equilibrium length and height in pure sand, 200 and 122 min, respectively, were needed to reach equilibrium in the sand that contained 7.4% clay. The

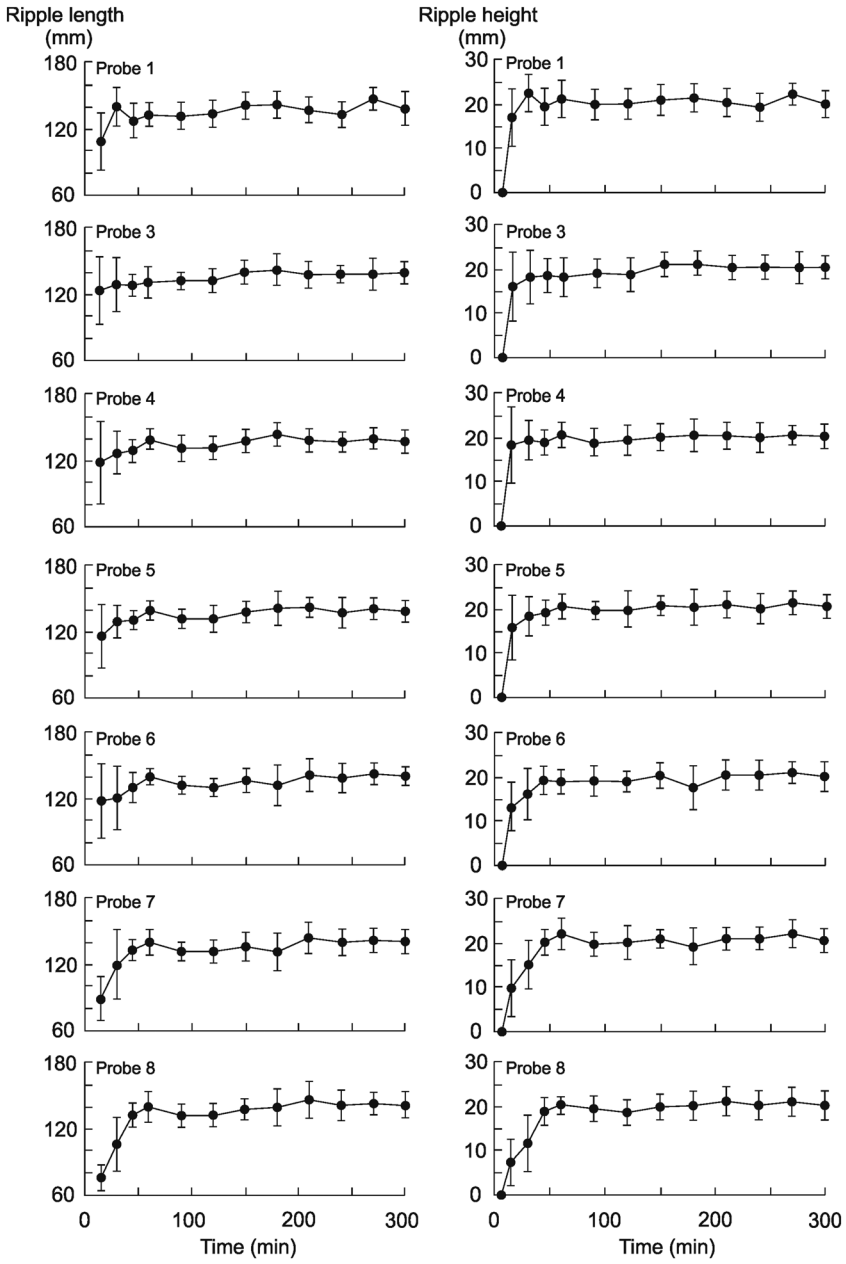


**Figure 7.** Development curves of wave ripple length and height in run 3 with 4.2% clay. The vertical black lines denote one standard deviation of the mean.

relatively large standard deviation of mean equilibrium time in runs 5 and 6 (Figures 10c and 10d) again reflects the slow expansion of the wave ripples across the bed.

### 3.3. Comparison of Pre- and Postexperiment Bed Sand Fractions

The pre- and postexperiment bed sand fractions are plotted against dimensionless depth below the sediment surface, $d/\eta_e$, in Figures 11a–11d, where $d$ is depth in core and $d/\eta_e = 0$ and $d/\eta_e = 1$ represent the equilibrium ripple crest and trough, respectively. Immediately below the equilibrium ripple crest, the mean sand fraction was 100% in all runs, that is, the sediment consisted of clay-free sand. Below this level, the mean sand fraction decreased rapidly, reaching values at or just above the preexperiment sand fractions at the level of the equilibrium ripple trough. Below the level of the equilibrium ripple trough, the mean sand fractions tended to be lower than the preexperiment values, especially in runs 4 and 6, but in run 3, the mean sand

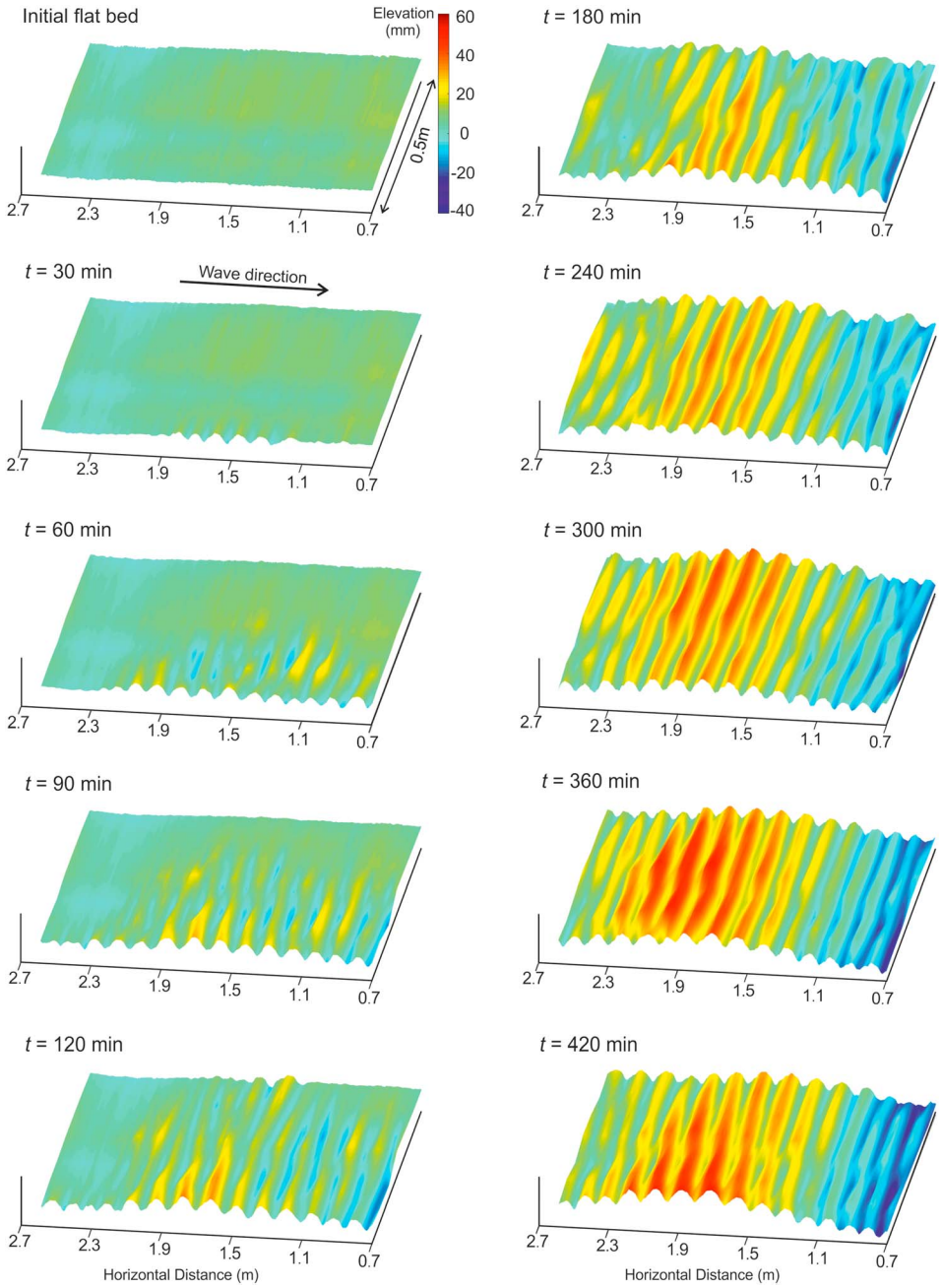


**Figure 8.** Three-dimensional bed scans showing the development of wave ripples in run 6 with 7.4% clay.

fractions remained close to the preexperiment values. At the base of each core, the mean sand fraction increased again to values at or just above the preexperiment sand fractions. The cores collected in the ripple troughs show a vertical trend in mean sand fraction similar to that at the ripple crest (Figures 11a–11d), except that the mean sand fraction was significantly lower immediately below the ripple trough and the lowest mean sand fractions, that is, the highest bed clay fractions, were present at a greater depth than below the ripple crest. In terms of mean bed clay fraction, the clay percentage decreased by $\leq$7.4% within the ripples and decreased by $\leq$5% and $\leq$3.3% down to ~35 mm below the equilibrium ripple crest and trough, respectively (Figures 11a–11d). Figure 11e shows the mean relative change in clay fraction, $\xi$, that is, the ratio of the clay fraction in core to the initial clay fraction averaged for runs 3 to 6, below the ripple crest and trough against dimensionless depth. In general, $\xi < 1$ between the ripple crests and

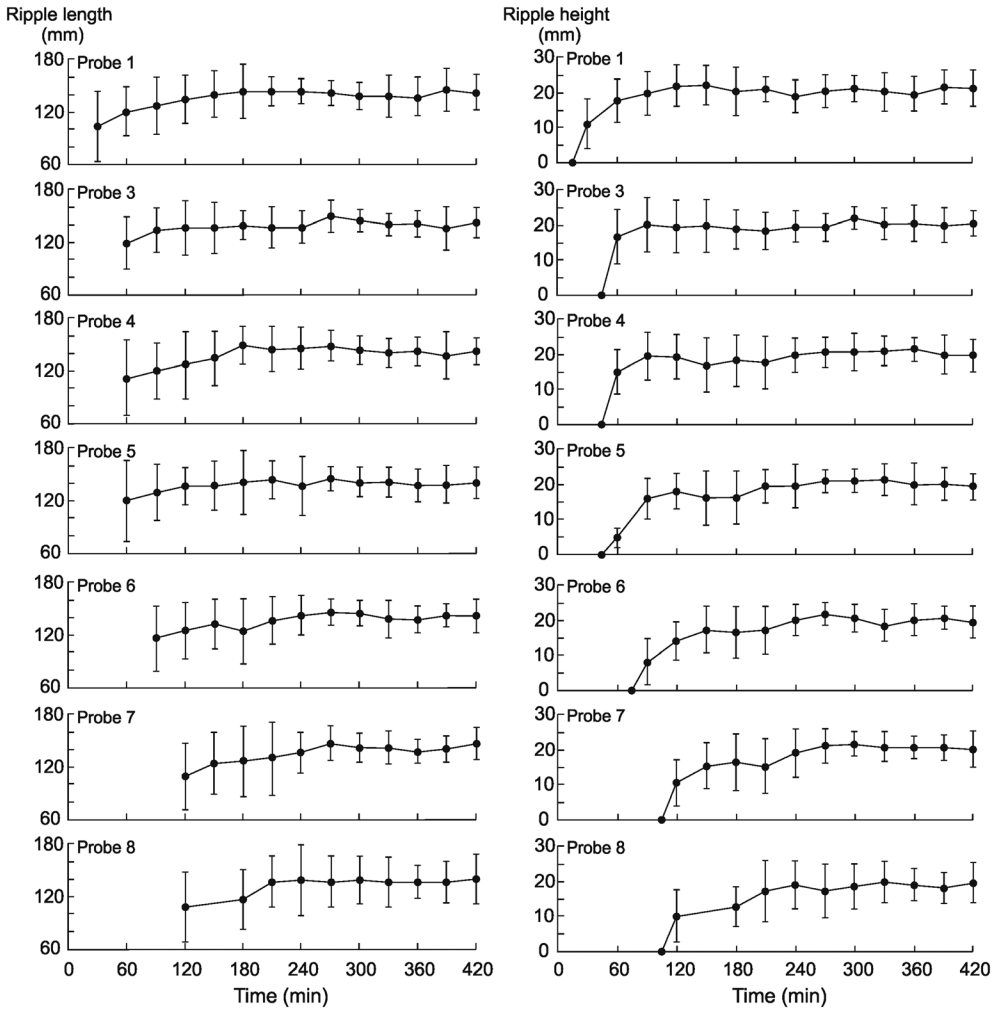


**Figure 9.** Development curves of wave ripple length and height in run 6 with 7.4% clay. The vertical black lines denote one standard deviation of the mean.

troughs, signifying that the wave ripples had lost clay at the end of the experiments. In contrast, the substrate immediately below the ripples had gained clay at the end of the experiments, with $\xi > 1$ for both the ripple crests and the ripple troughs.

## 4. Discussion

### 4.1. Wave Ripple Evolution in Cohesive Mixed Sand-Clay

The critical bed shear stress for sediment erosion has been found to significantly increase, and the erosion rate to decrease, if cohesive clay is added to a noncohesive sand bed, because the clay helps to establish electrochemical bonds between the sand particles (e.g., Alvarez-Hernandez, 1990; Collins, 1990; Mitchener & Torfs, 1996; Panagiotopoulos et al., 1997). Based on flume and field experiments, Mitchener and Torfs (1996) suggested that the properties of mixed sand-mud beds transform from cohesionless to cohesive with a gradually increase in mud fraction from 3% to 15% by weight. Panagiotopoulos et al. (1997) found that a clay fraction of 11% by weight is the threshold above which the clay changes the deposit structure, making the bed strongly resistant to erosion and decreasing the erosion rate. The present experimental results show that a relatively small increase in bed clay fraction from 0% to 4.2–7.4% is able to distinctly increase erosion resistance, which is consistent with these previous findings. Herein, this increase in erosion resistance was reflected in a progressively longer delay in the first appearance of the wave ripples on the initial flat bed, as the initial clay fraction within the sand was increased (Figure 9).

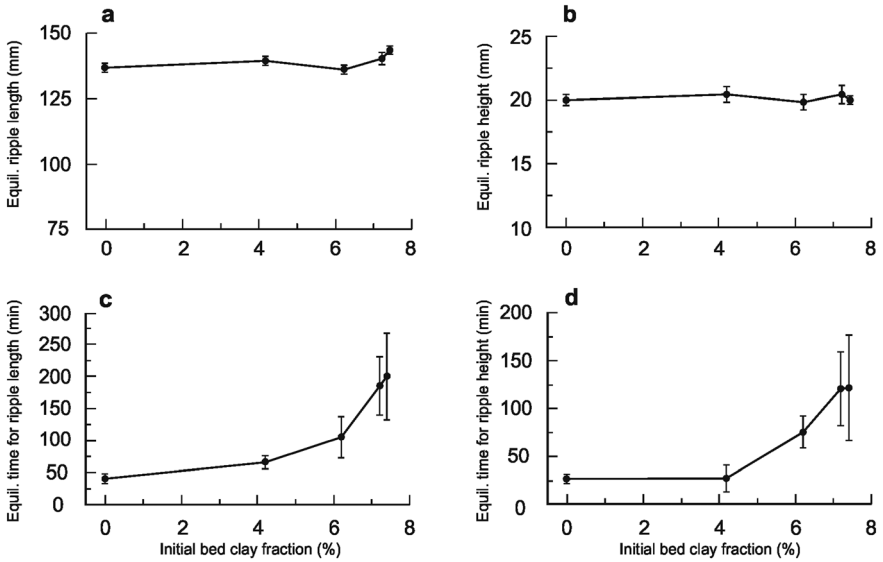


**Figure 10.** Equilibrium wave ripple (a) length and (b) height and equilibrium time for (c) length and (d) height against initial bed clay fraction for all experiments.

Our results also highlight the role of cohesive sediment on bed form dynamics by exponentially increasing the time the wave ripples required to reach 2-D shapes that span the channel width as a function of increasing bed clay fraction (Table 2). However, the equilibrium height and length of the wave ripples was found to be invariant with bed clay fraction. Under unidirectional flow, the dynamics of current ripples and dunes are also strongly affected by cohesive forces induced by clay (Baas et al., 2013; Schindler et al., 2015) and biological polymers (extracellular polymeric substances, EPSs; Malarkey et al., 2015; Parsons et al., 2016). A comparison of these data sets with those in the present study reveals similarities as well as differences in the dynamics of current-generated and wave-generated bed forms in cohesive sand. Malarkey et al. (2015) inferred from experimental data that the equilibrium height and length of current ripples are independent of bed EPS content, provided that sufficient time is available to reach equilibrium conditions. This is in agreement with the wave ripples in the present study. In contrast to the wave ripples herein, however, the size of dunes decreases rapidly, as the initial bed clay and EPS fraction are increased (Parsons et al., 2016; Schindler et al., 2015). Current ripples in mixed sand-clay were also smaller than in pure sand (Baas et al., 2013), but it cannot be ruled out that these current ripples were unable to reach equilibrium within the duration of the experiments of Baas et al. (2013), especially below a bed clay fraction of 13%. The current ripples of Baas et al. (2013) also started to form on the flat bed much sooner than the wave ripples in the present study; even at 13.8% clay, $t_f$ remained well below 0.5 hr (Baas et al., 2013). Once formed, the current ripples of Baas et al. (2013) reached their equilibrium height and length after similar periods of time, independent of bed clay fraction, whereas the wave-ripple equilibrium time increased rapidly with increasing bed clay fraction. These differences in development rate are inferred to result from differences in the spatial spreading of the bed forms on the flat bed. Currents tend to form incipient ripples at multiple locations on the bed, whereas the wave ripples herein were typically initiated at a single location (Figure 8). We hypothesize that currents are more efficient than waves in changing bed deficiencies into bed forms at similar forcing velocities (0.35 m/s in this study and 0.33–0.40 m/s in Baas et al., 2013). Once formed, current ripples have a higher migration rate than wave ripples (Bridge & Demicco, 2008), for which migration is limited to Stokes' drift, thus leading to a more rapid longitudinal and transverse spreading on the flat bed than the wave ripples. The higher migration rate may also be associated with a higher rate of advective transport of sediment, and a faster removal of clay from the bed, as discussed in more detail below.

These experimental results suggest that even small amounts of clay can greatly affect ripple development under waves. Wave ripples are important in sediment transport modeling (e.g., Soulsby, 1997; Warner et al., 2008), because these bed forms contribute to the suspension of sediment from the bed, and they constitute important bed roughness elements. Cohesive clay was found to delay the formation of wave ripples by

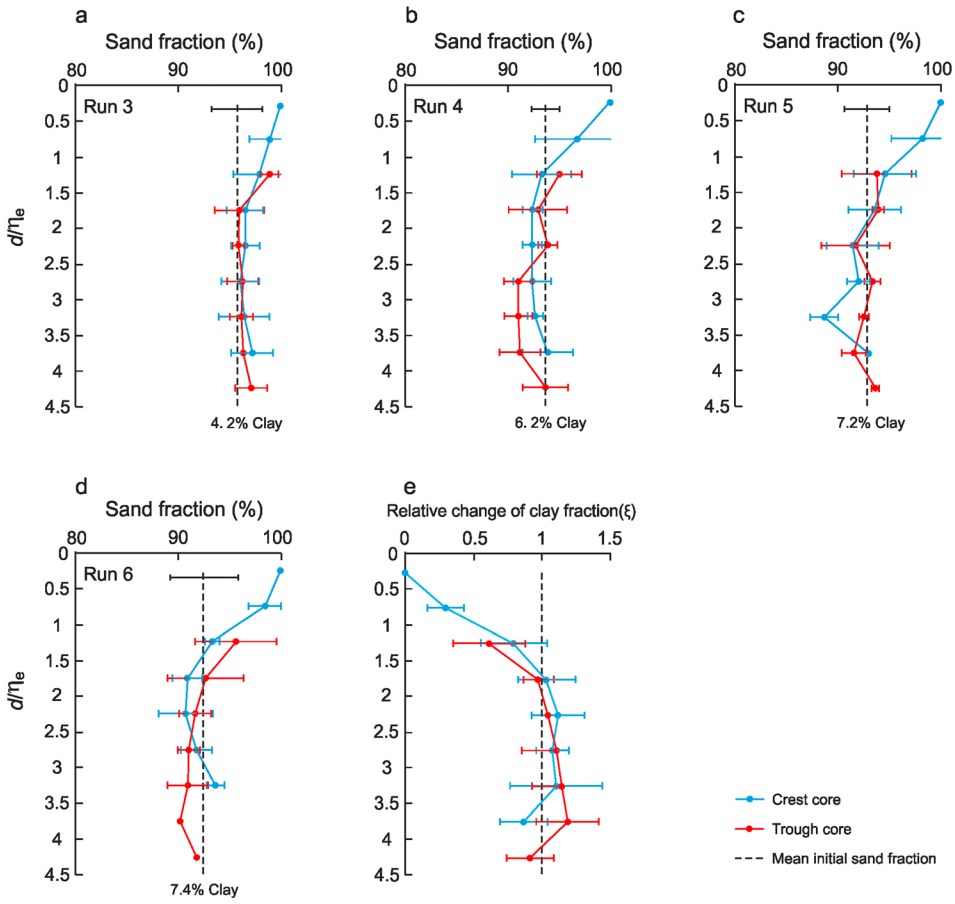


**Figure 11.** (a–d) Vertical changes in mean bed sand fraction in cores collected from ripple crests and troughs after each run. (e) Vertical relative changes in mean clay fraction of all crest and trough cores. The blue and red dots denote sand (a–d) and clay fraction (e) in ripple crest and trough, respectively. The vertical black dashed lines denote mean preexperiment sand fraction (a–d) and zero change in clay fraction (e). The blue, red, and black horizontal lines denote one standard deviation of the mean sand fraction for ripple crest, ripple trough, and initial bed, respectively. $d$ is core depth; $\eta_e$ is equilibrium ripple height; $\xi$ is relative clay fraction.

up to several hours, hence delaying the suspension of the fine sediment by the waves, and delay the development of full bed roughness. This hysteresis effect should be included in sediment transport models, even if the bed sediment appears to be dominated by sand, as 4–7% clay in sand is difficult to detect by eye. The slow development rate of wave ripples in mixed sand-clay may lead to an overestimation of bed roughness if pure-sand bed form predictors are used (e.g., Nelson et al., 2013; Traykovski, 2007) or an underestimation of the wave climate if wave ripple height and length are used to reconstruct wave parameters. Such predictions should be restricted to equilibrium wave ripples, since the experimental data suggest that the equilibrium height and length of wave ripples are independent of bed clay content. This hysteresis effect caused by the presence of cohesive clay is expected to be particularly important in estuaries, not only because clay is often more common in estuaries than in other shallow marine environments, such as on the shore-face, but also because waves may only be effective in causing wave ripple development during ebb and flood tides in a narrow period around high slack water, especially on mixed sand-mud intertidal flats. It is therefore hypothesized for the benefit of future field studies that nonequilibrium wave ripples will be more common in estuaries than on the shore-face, where often more time is available to form equilibrium wave ripples. Under wave conditions that are more energetic than in our flume experiments, the wave ripple development rate in mixed sand-clay may be increased, and the equilibrium time may be reduced, because of higher rate of winnowing of fines under higher bed shear stress (cf. equation (1)). In nature, however, wave ripple development is also controlled by sediment erodibility related to geochemical and biological properties of sediments (Grabowski et al.,

2011), for example, through the cohesive properties of EPSs of microphytobenthic origin (e.g., Malarkey et al., 2015; Parsons et al., 2016). Moreover, the suspension settling of clay particles in the form of mixed-sediment floccules has been found to affect the physical properties of the bed sediment (Manning et al., 2010, 2011), which, together with mixing of this cohesive sediment into the bed by benthic organisms, is also expected to influence bed form evolution. Therefore, further study is needed to fully quantify the effect of wave forcing and bed material properties on wave ripple development and stability.

### 4.2. Influence of Clay Removal on Wave Ripple Size

Previous flume studies found an inverse relationship between bed form size and bed clay fraction under unidirectional flow conditions (Baas et al., 2013; Schindler et al., 2015). However, the length ($L_e$~140 mm) and height ($H_e$~20 mm) of the wave ripples in the present study were independent of the initial bed clay faction, provided that the ripples were given enough time to reach their equilibrium size. It is inferred from the granulometric data presented in Figure 11 that the wave ripples transformed from mixed sand-clay bed forms to sand-rich bed forms during development by means of removal of the clay particles from the active surficial sediment layer. This removal process involved entrainment of clay into the water column and downward transfer of clay to depths below the active layer. Below, these processes are discussed in more detail.

Hydrodynamic forces are known to suspend fine particles from beds with a bimodal or multimodal grain size distribution, thereby leaving behind relatively coarse particles on the bed (e.g., Cizeau et al., 1999; Kleinhans, 2004; Lamb & Parsons, 2005; Liang et al., 2007). This sorting process, called winnowing (McCrone, 1963), enables current ripples in mixed clay-sand and EPS-sand to become increasingly sandy (Baas et al., 2013; Malarkey et al., 2015; Ye, 2016). Herein, clay winnowing is used to explain the invariance of equilibrium wave ripple height and length with initial bed clay fraction. As the waves winnowed the clay from the bed, the cohesive forces in the bed weakened and the wave ripples started to behave like bed forms in pure sand, especially close to and at equilibrium conditions. These waves were therefore able to scour the bed to the same depth as in pure sand, form equilibrium wave ripples with the same height and length as those in pure sand, and produce sandy bed forms on top of a mixed sand-mud substrate. In the present study, high winnowing efficiencies were recorded in the sediment cores that penetrated the ripple crests, culminating in 100% removal of clay immediately below the ripple crests. This winnowing efficiency under waves is much higher than under unidirectional flow, supported by the absence of pure sand at similar initial bed clay fractions in the experimental bed forms of Baas et al. (2013) and Ye (2016). This is consistent with the notion that wave-induced shear is more effective in entraining sediment than current-induced shear (Leeder, 2011; Soulsby, 1997).

The increase in clay fraction below the active surface layer (Figure 11) suggests that the clay particles were not only suspended into the oscillatory flow, but also moved downward into the substrate below the wave ripples. Estimations of clay loss from the ripples versus clay gain underneath the ripples, based on the data shown in Figure 11e, show that, on average, 30% of the clay may end up in the subsurface. Sato et al. (1984) and Cardenas et al. (2008) described pressure gradients across bed form profiles induced by high pressures at bed form troughs and low pressures at bed form crests, which set up water flow through the bed (Huettel et al., 1996). Moreover, the experiments of Huettel et al. (1996) under unidirectional flow demonstrated that these interstitial flows are able to carry suspended clay particles into the bed, where these particles settle in the pores between the sand particles. Previous papers also indicated that this interstitial flow enters the ripple trough in a downward direction and leaves the ripple crest in an upward direction under oscillatory flows (Precht & Huettel, 2004; Shum, 1993). Our experiments show that not only currents but also waves are capable of generating through-bed clay-laden flow; these clay particles moved deeper into the bed below the wave ripple troughs than below the wave ripple crests (Figure 11). Considering that the through-bed flow is driven by differences in height on the sediment surface, it is expected that similar downward movement and accumulation of clay particles is also possible under bed forms formed by combined waves and currents. Moreover, a sieving mechanism may have allowed the small clay particles to move downward into the substrate through gaps between the sand particles. We infer that the waves were strong enough to widen these gaps by periodically breaking the contacts between the sand particles during bed erosion and ripple migration. It is also feasible that interstitial flow facilitated this sieving mechanism, if the flow through the sediment reduced the packing density on its way from ripple trough to ripple crest.

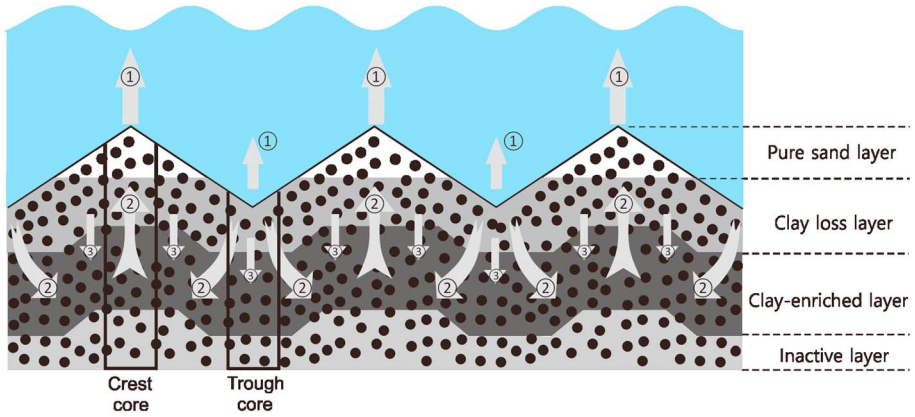


**Figure 12.** Conceptual model explaining the sedimentary texture of the rippled mixed sand-clay bed at equilibrium conditions. The horizons with different clay fractions are presented by different shades of gray, with the white and darkest gray colors denoting the pure sand layer and the clay-enriched layer, respectively. The gray arrows denote processes of clay removal: (1) clay winnowing; (2) clay-carrying interstitial flow; (3) sieving.

Further study is required to determine the precise contributions of interstitial flow and sieving to the movement of clay into the subsurface.

Figure 12 shows a conceptual model of the sediment texture within and below the wave ripples after reaching equilibrium at the end of the experiments. The ripple crests are dominated by pure sand, following strong winnowing of clay close to the sediment-water interface ("pure sand layer" in Figure 12). Underneath the pure sand layer, that is, around the base of the wave ripples and immediately below the ripple troughs, a "clay loss layer" (Figure 12) represents a progressively lower loss of clay compared to the initial bed clay fraction with increasing depth below the sediment surface. We infer that the clay was removed from this layer by a combination of winnowing and downward movement. The "clay-enriched layer" (Figure 12), which was up to 25 mm thick in the present experiments, depicts the depth range below the wave ripples where clay is added by interstitial flow and sieving. Below this layer, the final bed clay fraction resembles the initial bed clay fraction ("inactive layer" in Figure 12).

The clay-enriched layer beneath the wave ripples (Figure 12) can be considered as an armoring layer that helps stabilize the substrate and hinders the development of larger bed forms in, for example, a stronger wave climate. Our experiments reveal that the clay enrichment may take the bed clay fraction up to 10%, at which hysteresis effects (cf. Baas, 1994; Martin & Jerolmack, 2013; Paarlberg et al., 2010; Wilbers & Ten Brinke, 2003) should be even more important than in the present study, given the exponential increase in the timing of wave ripple development with increasing initial bed clay fraction (Figures 10c and 10d). This remarkable ability of waves to self-stabilize the bed by accumulating clay in the substrate is expected to further challenge the modeling of sediment transport, discussed above. Not only is the clay armoring likely to enhance hysteresis effects, but the presence of pure-sand bed forms is no guarantee that cohesive forces did not influence bed form development, given that the removal of clay has been shown herein to be a highly efficient process. However, the presence of mixed clay-sand below sandy wave ripples may be an indication of the development of the wave ripples from mixed sand-clay to pure sand, especially if a clay-enhanced layer —covering a layer with a lower clay fraction—is present immediately below the wave ripples.

Nutrients and chemical pollutants are often bound to clay particles (Horowitz, 1991, 2008; Svendsen et al., 1995). The displacement of clay particles from a mixed sand-clay bed by waves, either by release into the water column or by storage deeper into the bed, therefore has important implications for water-quality regulations in the coastal zone. The present study suggests that waves may release nutrients and pollutants with the clay particles into the water column. However, these chemical substances may also be stored for prolonged periods of time in a substrate that is able to withstand higher hydrodynamic forcing. Relatively small releases of nutrients into the water column are beneficial to aquatic ecosystems, but excessive release of nutrients and trace elements may lead to water pollution (e.g., Tyler et al., 2006), risking a serious threat to the coastal ecological balance. Storage of pollutants can be beneficial to the environment, but the

duration of storage needs to be considered, because a sudden release of enhanced concentrations of pollutants by strong waves or currents may lead to greater environmental problems than prolonged release of smaller quantities. The present data should fuel further studies to quantify the relative importance of these removal and storage processes for a wider range of flow and bed conditions.

## 5. Conclusions

The development rate and equilibrium size of wave ripples on mixed cohesive clay and cohesionless sand substrates under regular wave conditions were studied. Based on the results of the five large-scale flume experiments, the following conclusions are drawn:

1. A small increase in the bed clay fraction from 4.2% to 7.4% slowed down exponentially the development of the wave ripples on the initial flat bed; this included an increase in the timing of the first appearance of the wave ripples from several minutes to ~30 min. It thus appears that cohesive forces within the mixed sand-clay were able to produce strong bonds between sand grains, even at low bed clay fractions, and delay the growth of the wave ripples compared to those in pure sand.
2. Despite the clear difference in growth rate, the equilibrium length and height of the wave ripples of ~140 and ~20 mm, respectively, were independent of the initial bed clay fraction. Highly efficient removal of clay particles from the developing wave ripples by winnowing and sieving explains this independence.
3. The removal of clay by winnowing and sieving may have been complemented by pressure-driven, interstitial, clay-carrying flow between ripple troughs and ripple crests. In concert with the accumulation of clay by sieving, this resulted in the development of a clay-enriched layer beneath the wave ripples. This clay-rich layer may act as an armoring layer and render the bed more difficult to erode by subsequent wave forces. On average, 30% of the clay that was removed from the wave ripples ended up in the subsurface.

Given the low bed clay fractions (4.2% to 7.4%) at which wave ripple development was affected, as well as the exponential relationship between rippled development rate and bed clay fraction, nonequilibrium wave ripples are expected to be more common than equilibrium wave ripples in mixed-clay environments, such as estuaries, than accounted for previously. As a consequence, predictive models of sediment transport in modern environments and estimations of wave conditions in paleoenvironmental reconstructions need reassessment.

**Acknowledgments**
This work was part of the COHWAV project, supported by the Seventh Framework Programme of the European Community through a grant from the Integrating Activity HYDRALAB IV within the Transnational Access Activities program, under contract 261520. The authors highly appreciate the help and advice from Aaron Westlake, Nick Coultish, Brendan Murphy, Kim Rosewell, Reinier Schrijvershof, and Leiping Ye during the setup and execution of the flume experiments. All of data collecting from the flume experiments for this paper are available through the University of Hull digital repository (https://hydra.hull.ac.uk/resources/hull:16498).

## References

Alvarez-Hernandez, E. M. (1990). The influence of cohesion on sediment movement in channels of circular cross-section, (PhD thesis). University of Newcastle, UK.

Amoudry, L. O., & Souza, A. J. (2011). Deterministic coastal morphological and sediment transport modeling: A review and discussion. *Reviews of Geophysics*, *49*, RG2002. https://doi.org/10.1029/2010RG000341

Baas, J. H. (1994). A flume study on the development and equilibrium morphology of current ripples in very fine sand. *Sedimentology*, *41*(2), 185–209. https://doi.org/10.1111/j.1365-3091.1994.tb01400.x

Baas, J. H. (1999). An empirical model for the development and equilibrium morphology of current ripples in fine sand. *Sedimentology*, *46*(1), 123–138. https://doi.org/10.1046/j.1365-3091.1999.00206.x

Baas, J. H., Best, J. L., & Peakall, J. (2011). Depositional processes, bedform development and hybrid bed formation in rapidly decelerated cohesive (mud-sand) sediment flows. *Sedimentology*, *58*(7), 1953–1987. https://doi.org/10.1111/j.1365-3091.2011.01247.x

Baas, J. H., Davies, A. G., & Malarkey, J. (2013). Bedform development in mixed sand-mud: The contrasting role of cohesive forces in flow and bed. *Geomorphology*, *182*, 19–32. https://doi.org/10.1016/j.geomorph.2012.10.025

Bolaños, R., Thorne, P. D., & Wolf, J. (2012). Comparison of measurements and models of bed stress, bedforms and suspended sediments under combined currents and waves. *Coastal Engineering*, *62*, 19–30. https://doi.org/10.1016/j.coastaleng.2011.12.005

Bridge, J., & Demicco, R. (2008). *Earth surface processes, landforms and sediment deposits*. Cambridge: Cambridge University Press. https://doi.org/10.1017/CBO9780511805516

Cardenas, M. B., Cook, P. L., Jiang, H., & Traykovski, P. (2008). Constraining denitrification in permeable wave-influenced marine sediment using linked hydrodynamic and biogeochemical modelling. *Earth and Planetary Science Letters*, *275*, 127–137. https://doi.org/10.1016/j.epsl.2008.08.016

Cizeau, P., Makse, H. A., & Stanley, H. E. (1999). Mechanisms of granular spontaneous stratification and segregation in two-dimensional silos. *Physical Review E*, 59. https://doi.org/10.1103/PhysRevE.59.4408

Clifton, H. E., & Dingler, J. R. (1984). Wave-formed structures and paleoenvironmental reconstruction. *Marine Geology*, *60*(1–4), 165–198. https://doi.org/10.1016/0025-3227(84)90149-X

Collins, M. (1990). The behaviour of cohesive and non-cohesive sediments. Paper presented at the Proc. Int. Seminar Environment. Asp. Dredging Act. Port Autonome De Nantes Saint-Nazaire, Nantes, 15–32.

Flemming, B. W. (2002). Geographic distribution of muddy coasts. In T. Healy, Y. Wang, & J. A. Healy (Eds.), *Muddy coasts of the world processes, deposits and function. proceedings in marine science* (Vol. 4, pp. 99–201). Amsterdam: Elsevier. https://doi.org/10.1016/S1568-2692(02)80080-8

Grabowski, R. C., Droppo, I. G., & Wharton, G. (2011). Erodibility of cohesive sediment: The importance of sediment properties. *Earth-Science Reviews*, *105*(3–4), 101–120. https://doi.org/10.1016/j.earscirev.2011.01.008

Grant, W. D., & Madsen, O. S. (1982). Movable bed roughness in unsteady oscillatory flow. *Journal of Geophysical Research*, *87*(C1), 469–481. https://doi.org/10.1029/JC087iC01p00469

Grasmeijer, B., & Kleinhans, M. (2004). Observed and predicted bed forms and their effect on suspended sand concentrations. *Coastal Engineering*, *51*(5-6), 351–371. https://doi.org/10.1016/j.coastaleng.2004.05.001

Horowitz, A. J. (1991). *Primer on sediment-trace element chemistry*. MI: Lewis Publishers.

Horowitz, A. J. (2008). Determining annual suspended sediment and sediment-associated trace element and nutrient fluxes. *Science of the Total Environment*, *400*(1-3), 315–343. https://doi.org/10.1016/j.scitotenv.2008.04.022

Huettel, M., Ziebis, W., & Forster, S. (1996). Flow-induced uptake of particulate matter in permeable sediments. *Limnology and Oceanography*, *41*(2), 309–322. https://doi.org/10.4319/lo.1996.41.2.0309

Kleinhans, M. (2004). Sorting in grain flows at the lee side of dunes. *Earth-Science Reviews*, *65*(1-2), 75–102. https://doi.org/10.1016/S0012-8252(03)00081-3

Lamb, M. P., & Parsons, J. D. (2005). High-density suspensions formed under waves. *Journal of Sedimentary Research*, *75*(3), 386–397. https://doi.org/10.2110/jsr.2005.030

Leeder, M. (2011). *Sedimentology and sedimentary basins from turbulence to tectonics* (2nd ed.). Noida: Wiley-Backwell.

Li, M. Z., & Amos, C. L. (1998). Predicting ripple geometry and bed roughness under combined waves and currents in a continental shelf environment. *Continental Shelf Research*, *18*(9), 941–970. https://doi.org/10.1016/S0278-4343(98)00034-X

Liang, H., Lamb, M. P., & Parsons, J. D. (2007). Formation of a sandy near-bed transport layer from a fine-grained bed under oscillatory flow. *Journal of Geophysical Research*, *112*, C02008. https://doi.org/10.1029/2006JC003635

Malarkey, J., Baas, J. H., Hope, J. A., Aspden, R. J., Parsons, D. R., Peakall, J., et al. (2015). The pervasive role of biological cohesion in bedform development. *Nature Communications*, *6*(1), 6257. https://doi.org/10.1038/ncomms7257

Malarkey, J., & Davies, A. G. (2003). A non-iterative procedure for the Wiberg and Harris (1994) oscillatory sand ripple predictor. *Journal of Coastal Research*, *19*(3), 638–739.

Manning, A. J., Baugh, J. V., Spearman, J. R., Pidduck, E. L., & Whitehouse, R. J. (2011). The settling dynamics of flocculating mud-sand mixtures: Part 1—Empirical algorithm development. *Ocean Dynamics*, *61*(2–3), 311–350. https://doi.org/10.1007/s10236-011-0394-7

Manning, A. J., Baugh, J. V., Spearman, J. R., & Whitehouse, R. J. (2010). Flocculation settling characteristics of mud: Sand mixtures. *Ocean Dynamics*, *60*(2), 237–253. https://doi.org/10.1007/s10236-009-0251-0

Van der Mark, C., Blom, A., & Hulscher, S. J. (2008). Quantification of variability in bedform geometry. *Journal of Geophysical Research*, *113*, F000940. https://doi.org/10.1029/2007JF000940

Martin, R. L., & Jerolmack, D. J. (2013). Origin of hysteresis in bed form response to unsteady flows. *Water Resources Research*, *49*, 1314–1333. https://doi.org/10.1002/wrcr.20093

McCrone, A. W. (1963). Paleontology and biostratigraphy of the red eagle cyclothem (lower permian) in Kansas. *Kansas Geology Survey Bulletins*, *164*, 114.

Mitchener, H., & Torfs, H. (1996). Erosion of mud/sand mixtures. *Coastal Engineering*, *29*(1–2), 1–25. https://doi.org/10.1016/S0378-3839(96)00002-6

Nelson, T. R., Voulgaris, G., & Traykovski, P. (2013). Predicting wave-induced ripple equilibrium geometry. *Journal of Geophysical Research: Oceans*, *118*, 3202–3220. https://doi.org/10.1002/jgrc.20241

Nielsen, P. (1981). Dynamics and geometry of wave-generated ripples. *Journal of Geophysical Research*, *86*(C7), 6467–6472. https://doi.org/10.1029/JC086iC07p06467

O'Hara Murray, R., Thorne, P., & Hodgson, D. (2011). Intrawave observations of sediment entrainment processes above sand ripples under irregular waves. *Journal of Geophysical Research*, *116*, C01001. https://doi.org/10.1029/2010JC006216

Paarlberg, A. J., Dohmen-Janssen, C. M., Hulscher, S. J., Termes, P., & Schielen, R. (2010). Modelling the effect of time-dependent river dune evolution on bed roughness and stage. *Earth Surface Processes and Landforms*, *35*(15), 1854–1866. https://doi.org/10.1002/esp.2074

Panagiotopoulos, I., Voulgaris, G., & Collins, M. (1997). The influence of clay on the threshold of movement of fine sandy beds. *Coastal Engineering*, *32*(1), 19–43. https://doi.org/10.1016/S0378-3839(97)00013-6

Parsons, D. R., Schindler, R. J., Hope, J. A., Malarkey, J., Baas, J. H., Peakall, J., et al. (2016). The role of biophysical cohesion on subaqueous bed form size. *Geophysical Research Letters*, *43*, 1566–1573. https://doi.org/10.1002/2016GL067667

Pedocchi, F., & Garcia, M. (2009). Ripple morphology under oscillatory flow: 1. Prediction. *Journal of Geophysical Research*, *114*, C12014. https://doi.org/10.1029/2009JC005354

Perillo, M. M., Best, J. L., Yokokawa, M., Sekiguchi, T., Takagawa, T., & Garcia, M. H. (2014). A unified model for bedform development and equilibrium under unidirectional, oscillatory and combined-flows. *Sedimentology*, *61*(7), 2063–2085. https://doi.org/10.1111/sed.12129

Precht, E., & Huettel, M. (2004). Rapid wave-driven advective pore water exchange in a permeable coastal sediment. *Journal of Sea Research*, *51*(2), 93–107. https://doi.org/10.1016/j.seares.2003.07.003

Ruessink, G., Brinkkemper, J. A., & Kleinhans, M. G. (2015). Geometry of wave-formed orbital ripples in coarse sand. *Journal of Marine Science and Engineering*, *3*(4), 1568–1594. https://doi.org/10.3390/jmse3041568

Sato, S., Mimura, N., & Watanabe, A. (1984). Oscillatory boundary layer flow over rippled beds. Paper presented at the 19th Coastal Eng. Congress, Houston, USA. https://doi.org/10.1061/9780872624382.155

Schindler, R. J., Parsons, D. R., Ye, L., Hope, J. A., Baas, J. H., Peakall, J., et al. (2015). Sticky stuff: Redefining bedform prediction in modern and ancient environments. *Geology*, *43*(5), 399–402. https://doi.org/10.1130/G36262.1

Schretlen, J. J., Ribberink, J. S., & O'Donoghue, T. (2009). Sand transport under full-scale surface waves. In *Proceedings of coastal dynamics 2009: Impacts of human activities on dynamic coastal processes (with CD-ROM)* (pp. 1–13). Singapore: World Scientific. https://doi.org/10.1142/9789814282475_0123

Shum, K. T. (1993). The effects of wave-induced pore water circulation on the transport of reactive solutes below a rippled sediment bed. *Journal of Geophysical Research*, *98*(C6), 10,289–10,301. https://doi.org/10.1029/93JC00787

Soulsby, R. (1997). *Dynamics of marine sands: A manual for practical applications*. London: Thomas Telford.

Spearman, J. R., Manning, A. J., & Whitehouse, R. J. (2011). The settling dynamics of flocculating mud and sand mixtures: Part 2—Numerical modelling. *Ocean Dynamics*, *61*(2–3), 351–370. https://doi.org/10.1007/s10236-011-0385-8

Styles, R., & Glenn, S. M. (2002). Modeling bottom roughness in the presence of wave-generated ripples. *Journal of Geophysical Research*, *107*(C8), 3110. https://doi.org/10.1029/2001JC000864

Svendsen, L. M., Kronvang, B., Kristensen, P., & Græsbøl, P. (1995). Dynamics of phosphorus compounds in a lowland river system: Importance of retention and non-point sources. *Hydrological Processes*, *9*(2), 119–142. https://doi.org/10.1002/hyp.3360090202

Traykovski, P. (2007). Observations of wave orbital scale ripples and a nonequilibrium time-dependent model. *Journal of Geophysical Research*, *112*, C06026. https://doi.org/10.1029/2006JC003811

Tyler, A., Svab, E., Preston, T., Présing, M., & Kovács, W. (2006). Remote sensing of the water quality of shallow lakes: A mixture modelling approach to quantifying phytoplankton in water characterized by high-suspended sediment. *International Journal of Remote Sensing*, *27*(8), 1521–1537. https://doi.org/10.1080/01431160500419311

Van Rijn, L. C. (1993). *Principles of sediment transport in rivers, estuaries and coastal seas*. Amsterdam: Aqua Publications Amsterdam.

Van Rijn, L. C. (2007). Unified view of sediment transport by currents and waves. I: Initiation of motion, bed roughness, and bed-load transport. *Journal of Hydraulic Engineering*, *133*(6), 649–667. https://doi.org/10.1061/(ASCE)0733-9429(2007)133:6(649)

Warner, J. C., Sherwood, C. R., Signell, R. P., Harris, C. K., & Arango, H. G. (2008). Development of a three-dimensional, regional, coupled wave, current, and sediment-transport model. *Computers & Geosciences*, *34*(10), 1284–1306. https://doi.org/10.1016/j.cageo.2008.02.012

Wiberg, P. L., & Harris, C. K. (1994). Ripple geometry in wave-dominated environments. *Journal of Geophysical Research*, *99*(C1), 775–789. https://doi.org/10.1029/93JC02726

Wilbers, A., & Ten Brinke, W. (2003). The response of subaqueous dunes to floods in sand and gravel bed reaches of the Dutch Rhine. *Sedimentology*, *50*(6), 1013–1034. https://doi.org/10.1046/j.1365-3091.2003.00585.x

Williams, J., Bell, P., Thorne, P., Metje, N., & Coates, L. (2004). Measurement and prediction of wave-generated suborbital ripples. *Journal of Geophysical Research*, *109*, C02004. https://doi.org/10.1029/2003JC001882

Williams, J., Bell, P., Thorne, P., Trouw, K., Hardcastle, P., & Humphery, J. (2000). Observed and predicted vertical suspended sediment concentration profiles and bedforms in oscillatory-only flow. *Journal of Coastal Research*, *16*(3), 698–708.

Ye, L. (2016). Morphodynamics and suspended sediment transport in cohesive substrates. (unpublished PhD). University of Hull, Hull, UK.

Yokokawa, M. (1995). Combined-flow ripples: Genetic experiments and applications for geologic records. Memoirs of the Kyushu University, Faculty & Science, Series D, Earth & Planetary. *Sciences*, *29*, 1–38.